

## Article

# Unusual ‘Turn-on’ Ratiometric Response of Fluorescent Porphyrin-Pyrene Dyads to the Nitroaromatic Compounds

Irina I. Shepeleva <sup>1,\*</sup>, Kirill P. Birin <sup>1</sup>, Daria A. Polivanovskaia <sup>1</sup>, Alexander G. Martynov <sup>1</sup>,  
Alexander V. Shokurov <sup>1</sup>, Aslan Yu. Tsivadze <sup>1,2</sup>, Sofiya L. Selektor <sup>1</sup> and Yulia G. Gorbunova <sup>1,2,\*</sup>

<sup>1</sup> A.N. Frumkin Institute of Physical Chemistry and Electrochemistry, Russian Academy of Sciences, Leninsky Pr. 31, Bldg. 4, 119071 Moscow, Russia

<sup>2</sup> N.S. Kurnakov Institute of General and Inorganic Chemistry of Russian Academy of Sciences, Leninsky Pr. 31, 119991 Moscow, Russia

\* Correspondence: shepelevairene@gmail.com (I.I.S.); yulia@igic.ras.ru (Y.G.G.)

**Abstract:** Detection of nitroaromatic compounds (NAC) is an important task since these substances are hazardous to both the biosphere and the society. Fluorescent sensors developed for NAC detection usually demonstrate a ‘turn-off’ response to the analyte, while ‘turn-on’ sensors are rarely reported. Here, we present a showcase report on new pyrene-imidazoporphyrin dyads that demonstrate an unusual analytic response to NAC with clear ‘turn-on’ behavior followed by an unexpected appearance of a new band, which can be ascribed to exciplex emission. The porphyrin backbone of the dyad also allows registration of its own fluorescence, providing an internal reference signal for ratiometric detection. The association constants in the order of  $10^4 \text{ M}^{-1}$  are reported.

**Keywords:** porphyrin; nitroaromatic; chemosensor; fluorescence; intramolecular rotation; turn-on sensor; pyrene; ratiometric



**Citation:** Shepeleva, I.I.; Birin, K.P.; Polivanovskaia, D.A.; Martynov, A.G.; Shokurov, A.V.; Tsivadze, A.Y.; Selektor, S.L.; Gorbunova, Y.G. Unusual ‘Turn-on’ Ratiometric Response of Fluorescent Porphyrin-Pyrene Dyads to the Nitroaromatic Compounds. *Chemosensors* **2023**, *11*, 43. <https://doi.org/10.3390/chemosensors11010043>

Academic Editors: Lintao Zeng and Minhuan Lan

Received: 28 November 2022

Revised: 24 December 2022

Accepted: 26 December 2022

Published: 3 January 2023



**Copyright:** © 2023 by the authors. Licensee MDPI, Basel, Switzerland. This article is an open access article distributed under the terms and conditions of the Creative Commons Attribution (CC BY) license (<https://creativecommons.org/licenses/by/4.0/>).

## 1. Introduction

Nitroaromatic compounds (NAC) are widely used in a large number of chemical industries as dyes, herbicides, insecticides, solvents, and, most prominently, explosives. The introduction of the nitro group into aromatic rings imparts strong polarization of the molecule, inhibits further electrophilic substitution of the benzene ring and also provides a number of unique physical and chemical properties, which explains their aforementioned popularity [1–3]. At the same time, these very properties are responsible for what NAC are notorious for—environmental pollution [4], danger to living organisms’ well-being [5–7], and comprising a huge part of man-made explosives jeopardizing public safety [8]. All the described NAC features set a crucial challenge for modern chemistry and materials science: we have to be able to detect the NAC traces in imperceptible amounts in the atmosphere, industrial plants, and potential locations of traumatizing NAC usage before these compounds accumulate enough to result in damage. To date, there is a number of diverse ways to detect the NAC both directly and indirectly [9–15], and among them, the state-of-the-art research in chemistry belongs to chemosensors, i.e., molecular structures capable of analyte recognition and analytical signal generation [16–18]. These chemosensors are especially of great interest thanks to their ability of recognition at the molecular level, great potential for miniaturization, and integration into electronic devices that could be equally applied under all kinds of conditions (NAC detection in gas, solid, or liquid phase) [19]. Particularly, fluorescent sensors remain the most studied systems due to their simplicity of use, fast response, and high sensitivity in detection, while allowing both qualitative and quantitative determination of the analyte [20].

Fluorescent NAC molecular sensors usually utilize either ‘turn-on’ or ‘turn-off’ mechanisms of action [21–23], depending on the type of interaction between the analyte and single sensing fluorescent molecule. It should be noted that in the case of ‘turn-off’ sensors

it is not always clear that the fluorescent signal is quenched by the target analyte, and is not just inhibited by the inner filter effect, deterioration of the fluorophore or its removal from the sensory platform, which makes calibration and employment with real samples difficult [24,25]. In this regard, the ‘turn-on’ sensing scheme seems far more promising, yielding a distinct signal. However, it is rare that a non-selective interaction leads to the enhancement of the fluorescent signal [26–28]. Nevertheless, implementation of this concept is much more complicated, usually requiring complex molecular architecture of the chemosensor [29,30].

An approach that can level off the disadvantages of single-fluorophore sensor concepts is to develop sensors based on the compounds containing more than one fluorophore. The fluorophore constituents of such systems can interact with each other via photoinduced electron transfer (PET), intramolecular charge transfer (ICT), or non-radiative energy transfer (NRET) [31–38]. Thus, the resulting fluorescence spectra of such compounds contain signals from several fluorophores, intensities of which are tied not only to the fluorophores themselves, but also to the efficiency of the energy transfer between them, which in turn can be governed by the analyte binding. This can provide an enhanced analytic response, an internal fluorescent reference, or even multimodal detection pathways [39].

It can be emphasized that processes mentioned above are quite often realized in derivatives of polycyclic aromatic hydrocarbons (PAH) bearing extended  $\pi$ -electron systems [40–42]. Given the fact that the PAH photophysical properties could be extremely sensitive to their environment and solvent polarity, it is not surprising that they have found their use in the field of chemosensors and sensing devices [43–45]. More often, PAH derivative sensors provide the ‘turn-off’ response to the bound nitroaromatic compounds, which is associated with the electron transfer from the PAH part to the nitroaromatic molecule due to  $\pi$ - $\pi$  stacking [46–50]. However, it is worth noting that some sensors based on PAH are able to respond in the ‘turn-on’ way [44,51–53] as well. In addition, the ratiometric sensors based on the PAH-derivatives are also known [54–57].

In our previous work we studied nickel(II) pyrenyl-imidazoporphyryr dyad **NiPIP** [58], whose fluorescence from both porphyrin and pyrenyl units was completely quenched because of the presence of nickel metal center, suggesting the efficient intramolecular communication between these units. In the present work, we decided to use the advantage of this communication in similar bimodal dyads—**H<sub>2</sub>PIP** and **ZnPIP**, which do not contain quenching metal centers. Initially, we envisioned the generation of the analytic response via modulation of NRET from the pyrene fragment to the porphyrin core due to pyrene fluorescence quenching upon stacking with NAC. However, the first experimental measurements have shown quite unexpected results: instead of pyrene emission quenching, we observed the inverse, while porphyrin emission was wholly unaffected. Thus, we investigate the potential of the discovered effect as a new analytic signal generation modality, on example of detection of several NAC species.

## 2. Materials and Methods

### 2.1. Materials

All chemicals and starting materials were obtained commercially from Acros or Sigma and used without further purification. **NiPIP** [58] and 2-(1-pyrenyl) benzimidazole **BIP** [59] were synthesized following the published protocols. The solvents were treated following the standard procedures [60]. The analytes solutions were made by dissolving of solid analytes in toluene. We dissolved 1.22 mg of **TNP** in 7.5 mL of toluene to get **TNP** solution with concentration of  $7.1 \times 10^{-4}$  M and 1  $\mu$ L of **NB** in 12.5 mL of toluene to provide **NB** solution with concentration of  $7.8 \times 10^{-4}$  M (Figure S1 in Supplementary Information).

**Preparation of H<sub>2</sub>PIP.** **NiPIP** (70 mg, 0.06 mmol) was dissolved in TFA (1.67 mL), H<sub>2</sub>SO<sub>4</sub> (422  $\mu$ L) was added upon vigorous stirring and the resulting mixture was stirred for 10 min at room temperature. Afterwards the mixture was diluted with CH<sub>2</sub>Cl<sub>2</sub> (20 mL) and neutralized with saturated solution of NaOAc in water. The organic phase was separated, evaporated and the target compound was isolated by column chromatography at silica gel

with hexane/DCM mixtures (0→80% of DCM) used as eluents. The subsequent purification by gel permeation chromatography provided 20 mg (30%) of **H<sub>2</sub>PIP**.

<sup>1</sup>H NMR (CDCl<sub>3</sub>; δ, ppm; J, Hz): 9.76 (d, 1H, <sup>3</sup>J = 9.3, H<sub>PyR</sub>), 9.08 (d, 1H, <sup>3</sup>J = 4.7 Hz, H<sub>β</sub>), 9.00 (d, 3H, <sup>3</sup>J = 4.9, 2H<sub>β</sub>+NH), 8.96 (d, 1H, <sup>3</sup>J = 4.7, H<sub>β</sub>), 8.83 (s, 2H, H<sub>β</sub>), 8.32 (d, 1H, <sup>3</sup>J = 8.4, H<sub>PyR</sub>), 8.29 (d, 2H, <sup>3</sup>J = 7.3 Hz, *ms*-H<sub>O-Ar</sub>), 8.28 (d, 1H, <sup>3</sup>J = 7.4, H<sub>PyR</sub>), 8.25–8.20 (m, 4H, 2 × *ms*-H<sub>O-Ar</sub>+2H<sub>PyR</sub>), 8.17–8.11 (m, 7H, 4 × *ms*-H<sub>O-Ar</sub>+3H<sub>PyR</sub>), 8.11–8.07 (m, 2H, H<sub>PyR</sub>), 7.49 (d, 2H, <sup>3</sup>J = 8.1, *ms*-H<sub>m-Ar</sub>), 7.45 (d, 2H, <sup>3</sup>J = 8.0, *ms*-H<sub>m-Ar</sub>), 7.30 (d, 2H, <sup>3</sup>J = 7.0, *ms*-H<sub>m-Ar</sub>), 7.29 (d, 2H, <sup>3</sup>J = 7.0, *ms*-H<sub>m-Ar</sub>), 4.32 (t, 2H, <sup>3</sup>J = 6.7, CH<sub>2</sub>O), 4.32–4.24 (m, 6H, CH<sub>2</sub>O), 2.08–1.95 (m, 8H, CH<sub>2</sub>), 1.73–1.64 (m, 8H, CH<sub>2</sub>), 1.15–1.09 (m, 9H, CH<sub>3</sub>), 1.06 (t, <sup>3</sup>J = 7.4, 3H), –2.81 (s, 2H, NH<sub>inner</sub>).

<sup>13</sup>C NMR (CDCl<sub>3</sub>; δ, ppm): 159.88, 159.50, 159.20, 152.23, 135.72, 135.66, 134.82, 134.74, 134.59, 134.31, 133.91, 131.93, 131.67, 131.31, 129.43, 128.73, 128.48, 127.41, 126.99, 126.40, 125.73, 125.64, 125.44, 125.10, 124.89, 124.80, 121.14, 120.92, 117.68, 114.71, 114.23, 113.32, 112.91, 112.86, 68.47, 68.20, 68.12, 31.97, 31.75, 31.63, 19.75, 19.61, 19.59, 14.18, 14.15, 14.12.

MALDI-TOF MS: *m/z* calcd. for C<sub>77</sub>H<sub>70</sub>N<sub>6</sub>O<sub>4</sub> [M]<sup>+</sup> 1142.55, found 1142.46.

UV-vis (CHCl<sub>3</sub>; λ<sub>max</sub>, nm; log(ε)): 281 (4.47), 424 (5.53), 520 (4.36) 556 (4.06), 588 (3.94), 651 (3.57).

**Preparation of ZnPIP.** **H<sub>2</sub>PIP** (10 mg, 8.7 μmol) was dissolved in 9:1 CHCl<sub>3</sub>/MeOH mixture (10 mL), Zn(OAc)<sub>2</sub> (8 mg, 44 μmol) was added and the mixture was stirred overnight at room temperature shielded from light. Upon complete conversion the mixture was evaporated to dryness and purified by flash chromatography at silica gel with DCM→DCM/MeOH (1 vol.% of MeOH) used as eluents that provided 8.5 mg (83%) of **ZnPIP**.

<sup>1</sup>H NMR (20%MeOD in CDCl<sub>3</sub>; δ, ppm; J, Hz): 9.73 (d, 1H, <sup>3</sup>J = 9.3, H<sub>PyR</sub>), 9.05 (br.s, 1H, H<sub>β</sub>), 9.00 (d, 2H, <sup>3</sup>J = 4.3, H<sub>β</sub>), 8.94 (br.s, 1H, H<sub>β</sub>), 8.93 (s, 2H, H<sub>β</sub>), 8.28 (d, 2H, <sup>3</sup>J = 9.2, *ms*-H<sub>O-Ar</sub>+H<sub>PyR</sub>), 8.26–8.17 (m, 5H, 3 × *ms*-H<sub>O-Ar</sub>+2 × H<sub>PyR</sub>), 8.13 (d, 5H, <sup>3</sup>J = 7.7, 4 × *ms*-H<sub>O-Ar</sub>+H<sub>PyR</sub>), 8.10 (d, 1H, <sup>3</sup>J = 8.8, H<sub>PyR</sub>), 8.08–8.03 (m, 2H, H<sub>PyR</sub>), 7.43 (d, 4H, <sup>3</sup>J = 7.7, *ms*-H<sub>m-Ar</sub>), 7.26 (d, 4H, <sup>3</sup>J = 7.9, *ms*-H<sub>m-Ar</sub>), 4.27 (m, 8H, CH<sub>2</sub>O), 1.97 (m, 8H, CH<sub>2</sub>), 1.66 (hept, 8H, <sup>3</sup>J = 7.6, CH<sub>2</sub>), 1.11 (t, 12H, <sup>3</sup>J = 7.4, CH<sub>3</sub>). Imidazole NH-proton resonance is not observed as a result of exchange with MeOD.

<sup>13</sup>C NMR (20%MeOD in CDCl<sub>3</sub>; δ, ppm): 159.49, 159.03, 152.02, 151.85, 150.31, 149.79, 149.39, 149.18, 140.04, 139.15, 135.79, 135.52, 134.23, 132.13, 131.81, 131.52, 131.24, 131.15, 131.01, 129.83, 129.32, 128.60, 128.35, 127.28, 126.84, 126.29, 125.54, 125.52, 125.31, 125.20, 124.80, 124.72, 124.63, 121.63, 117.81, 115.13, 113.89, 112.96, 112.52, 68.14, 31.68, 19.51, 14.05. Some resonances are not observed as a result of considerable broadening of the signals.

MALDI-TOF MS: *m/z* calcd. for C<sub>77</sub>H<sub>68</sub>N<sub>6</sub>O<sub>4</sub>Zn [M]<sup>+</sup> 1204.46, found 1204.31.

UV-vis (PhMe; λ<sub>max</sub>, nm; log(ε)): 294 (4.53), 358 (4.43), 430 (5.47), 551 (4.41), 591 (4.14).

## 2.2. UV-Vis and Fluorescence Titration

The UV-vis and fluorescence titration experiments were carried out in the wavelength range of 220–900 nm using a Shimadzu UV-2450 PC spectrophotometer (Japan) and a Shimadzu RF-5301 PC fluorimeter (Japan), respectively. An excitation wavelength of the **D** moiety was 346 nm, the excitation wavelengths of the **A** moiety were 519 nm and 550 nm for **H<sub>2</sub>PIP** and **ZnPIP**, respectively, unless stated otherwise.

The concentrations of **H<sub>2</sub>PIP** and **ZnPIP** were determined according to Beer–Lambert law using extinction coefficient (ε) known in every case. Thus, for each set (UV-vis and fluorescence) of titration experiments, the solutions of **H<sub>2</sub>PIP** (log(ε) = 5.51 (426 nm) in toluene), **ZnPIP** (log(ε) = 5.47 (431 nm) in toluene) at concentrations in the range of 7.3–9.0 × 10<sup>−7</sup> M were prepared by dissolving in toluene of a certain volume in a quartz cuvette (1 cm path length) right before the titration.

The titration with one of the analytes of **H<sub>2</sub>PIP** or **ZnPIP** solution was accomplished by the addition of the analyte molar equivalents in the cuvette using a chromatographic syringe. In the case of **H<sub>2</sub>PIP** (7.7 × 10<sup>−7</sup> M) titration with **NB** solution, the volume of 1 equivalent (V<sub>1eq</sub>) was equal to 2.5 μL; the addition of **NB** solution was in the range of

2.5–500.0  $\mu\text{L}$ . In the case of **ZnPIP** ( $7.3 \times 10^{-7}$  M) the addition of **NB** ( $V_{1\text{eq}} = 2.4 \mu\text{L}$ ) solution was in the range of 2.4–724.8  $\mu\text{L}$ . The addition of **TNP** solution to **ZnPIP** ( $7.9 \times 10^{-7}$  M) was in the range of 2.8–543.2  $\mu\text{L}$ .

All the titration spectra presented in the work are corrected for dilution effects and second order of diffraction artefacts (Figure S2). Association constants were determined using Bandfit online tool available at <http://supramolecular.org> (accessed on 24 December 2022) [61].

### 2.3. “ZnPIP in PMMA” Film Preparation

A total of 6.11 g of **PMMA** ( $M_w \sim 15000$ ) powder was dissolved in 12 mL of toluene under constant stirring and heating at 100 °C using IKA C-MAG HS 10 hotplate stirrer (Germany). A total of 8.6 mL of the obtained 30% *v/v* **PMMA** solution was mixed with 4.3 mL of a **ZnPIP** solution ( $1.8 \times 10^{-5}$  M) in toluene, resulting in the final **PMMA** concentration of 20% *v/v*. The mixture was poured into a PTFE Petri dish and left for 48 h for toluene to evaporate. The final **ZnPIP** concentration was ca 0.004% *w/v* in the dried polymer film.

For the absorbance and fluorescence spectra measurements, the solid film sample was fixed in a sample holder at 90° and 45° to the light source, respectively.

### 2.4. Quantum Chemical Calculations

All calculations were performed using ORCA 5.0.3 quantum chemical package [62]. Geometry optimization was performed using the “Swiss army knife” composite electronic-structure method— $r^2\text{SCAN-3c}$  [63]. Solvation effects in toluene media were accounted within CPCM model [64].

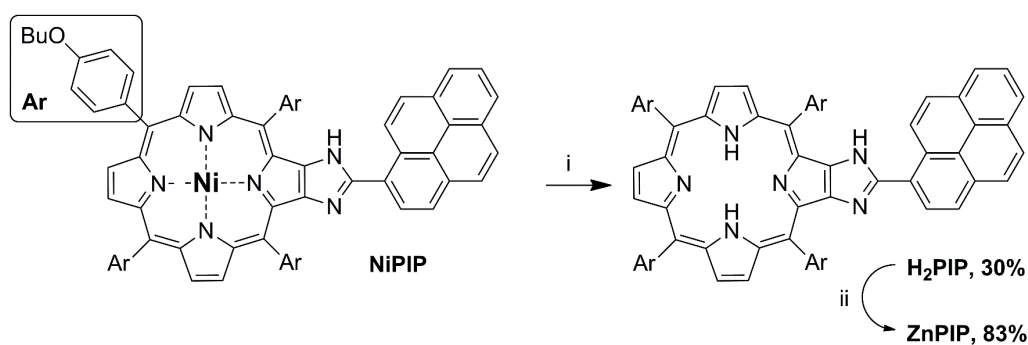
Gabedit 2.3.0 program was used to prepare the input files and to follow the progress of the calculations, and the Chemissian 4.65 program (by L. Skripnikov) was used to analyze and visualize the results of the quantum-chemical calculations [65]. For the current version see [www.chemissian.com](http://www.chemissian.com), (accessed on 27 November 2022).

Reduced density gradient (RDG) analysis and calculations within Quantum theory of atoms in molecules (QTAIM) were performed using Multiwfn 3.8 (dev) [66]. VMD 1.9.4 [67] was used for visualization. Calculations were performed using CAM-B3LYP/6-31(d) wavefunctions [68,69].

## 3. Results

The previously reported non-emissive pyrene-appended dyad **NiPIP** [58] was subjected to derivatization with the aim of modification of its photophysical properties (Scheme 1). The low yield of **H<sub>2</sub>PIP** upon demetalation of **NiPIP** is caused by the degradation of the porphyrin macrocycle under the reaction conditions. It could be presumed that the bulkiness of the neighboring porphyrin and pyrene fragments facilitates the degradation of the imidazole moiety. This is circumstantially proven by the presence of the components with blue luminescence in the reaction mass detected by TLC, which could be attributed to pyrene derivatives, which nevertheless could be successfully separated by chromatography. The metalation of the free-base **H<sub>2</sub>PIP** provided the corresponding Zn(II) complex **ZnPIP**.

First, spectral characterization of the studied dyads was carried out. The **H<sub>2</sub>PIP** absorbance spectrum (the black curve in Figure 1) exhibits weak bands around 300–346 nm attributed to a pyrenyl unit absorbance and intense Soret band at 426 nm together with four Q bands at 519, 555, 590, and 653 nm related to the porphyrin unit absorbance. The absorbance spectrum of **ZnPIP** is similar to the **H<sub>2</sub>PIP** one (the black curve in Figure 2), except for a shift of the Soret band to 431 nm and a fewer number of Q bands, which is typical for regular metal complexes of porphyrins as compared to their free-base analogues [70,71]. The Q bands of **ZnPIP** are located at 550 and 590 nm, respectively.



**Scheme 1.** Transformations of the porphyrin-pyrene dyads. i: H<sub>2</sub>SO<sub>4</sub>, TFA, r.t.; ii: Zn(OAc)<sub>2</sub>, CHCl<sub>3</sub>/MeOH, r.t.

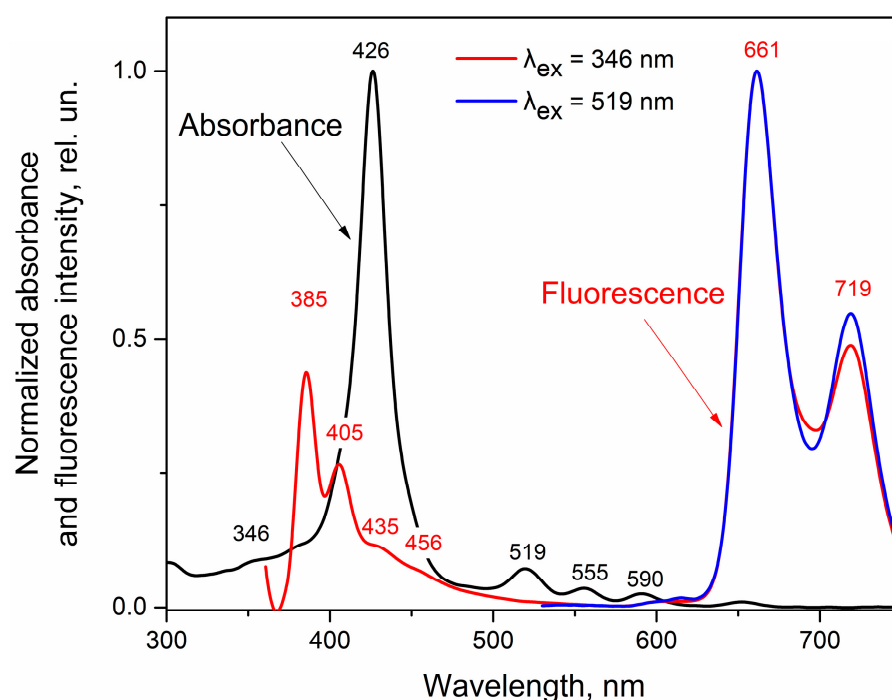


**Figure 1.** The normalized by maximum UV-vis absorbance and fluorescence spectra of H<sub>2</sub>PIP in toluene.

Both H<sub>2</sub>PIP and ZnPIP show dual emission from both pyrene and porphyrin units (red and blue curves in Figures 1 and 2). The direct excitation of porphyrin moiety of H<sub>2</sub>PIP (the blue curve in Figure 1) leads to its emission bands at 661 and 719 nm. The fluorescence spectrum of H<sub>2</sub>PIP upon 346 nm excitation (the red curve in Figure 1) shows the pyrenyl bands at 385 and 405 nm together with less pronounced shoulders at 435 and 456 nm as well as bands at 661 and 719 nm belonging to the porphyrin emission. The spectral overlap between the mentioned region of pyrene emission and Soret band absorbance could be the reason for NRET between the pyrene and porphyrin fragments and, subsequently, such porphyrin fluorescence. Therefore, further in the text we use the letters **D** (for energy donor) and **A** (for energy acceptor) to refer to the pyrene and porphyrin moieties of the dyads, respectively. Such distinction makes the description of photophysical phenomena related to energy transfer easier. At the same time, it should be noted that it is characteristic for porphyrins to have a small intrinsic fluorescence response upon irradiation by light in the near UV-region (see Figure S3 and [72] as an example).

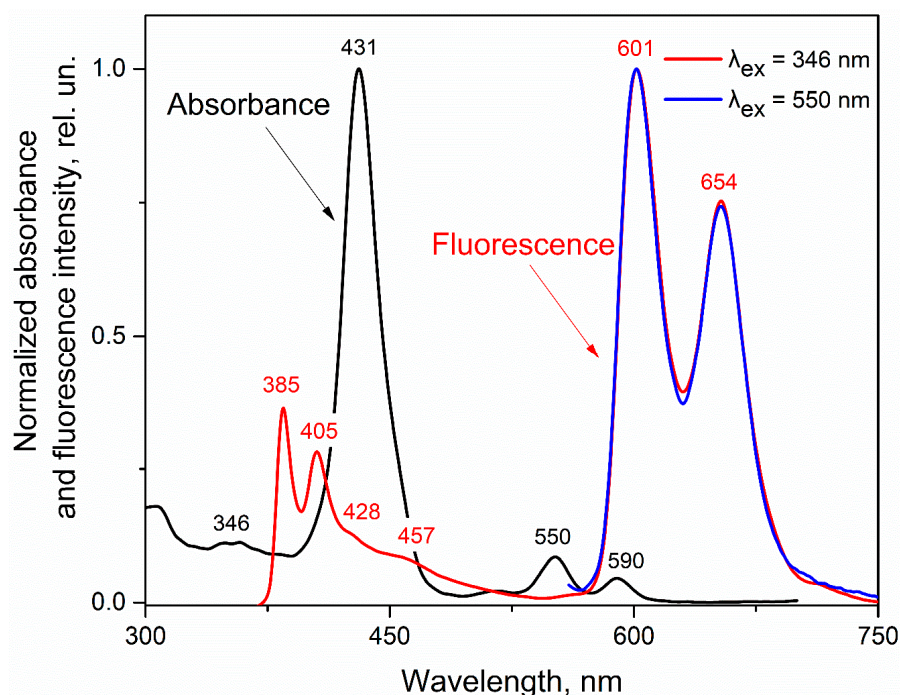


**Figure 2.** The normalized by maximum UV-vis absorbance and fluorescence spectra of **ZnPIP** in toluene.

The **ZnPIP** fluorescence spectra (the red and blue curves in Figure 2) are identical to the **H<sub>2</sub>PIP** ones apart from the porphyrin emission bands being shifted to 601 and 654 nm under excitation at both 346 and 550 nm. Barely visible shoulders of **D** emission are observed at 428 and 460 nm when **ZnPIP** is excited at 346 nm (instead of 435 and 456 nm in the **H<sub>2</sub>PIP** case). The spectral overlap between the **A** absorbance and **D** emission has almost not changed, indicating the potential of NRET occurring between these units.

The observed spectra demonstrate that the **D** and **A** moieties of **H<sub>2</sub>PIP** and **ZnPIP** are able to fluoresce as independent or partially dependent fluorophores. Therefore, concerning the highlighted spectral characteristics of both dyads, we can focus on the set of their fluorescence bands that can further be used in quantifying the interaction with analytes. To do this, we aim to use numerical values of the emission peak intensities for both **D** and **A**, being generated upon various excitation conditions at various concentrations of the added analyte. Schematic showing the parts of the dyad that are excited and which emission is measured in each specific case is provided in Figure 3. First, by exciting the dyads in the **D** absorbance wavelength (346 nm), it is possible to record the intrinsic **D** emission in the region of 385–460 nm, which will be denoted as a **D-D** value (Figure 3a). Then, the direct excitation of the porphyrin fragment (in 519 nm for **H<sub>2</sub>PIP** and 550 nm for **ZnPIP**) yields its independent fluorescence at 661 or 601 nm for **H<sub>2</sub>PIP** and **ZnPIP**, respectively, which can be marked as **A-A<sub>direct</sub>** (Figure 3b). Finally, since the **D** excitation at 346 nm also generates the **A** emission, potentially resulting from NRET, we mark such emission as **D-A<sub>NRET</sub>** (Figure 3c).

Previously reported NAC sensors based on pyrene receptor units typically demonstrated ‘turn-off’ sensing, where pyrene fluorescence is quenched by stacking with the analyte [46,47,73–79]. We assumed that in our dyads, where the pyrene moiety seemed to be an energy donor and the porphyrin moiety—an acceptor, the analogous pyrene quenching would be observed. In this case, the NRET process would weaken upon analyte detection, as in other pyrene-based NAC sensors utilizing NRET [80]. Consequently, the porphyrin fluorescence attributed to NRET from the pyrene should quench, while the intrinsic porphyrin emission (when it is directly excited through its own light absorbance) should remain the same. Moreover, rotations, vibrations, aggregation, as well as other

possible photophysical phenomena can also be affected by the interaction of the pyrene part with the analyte.

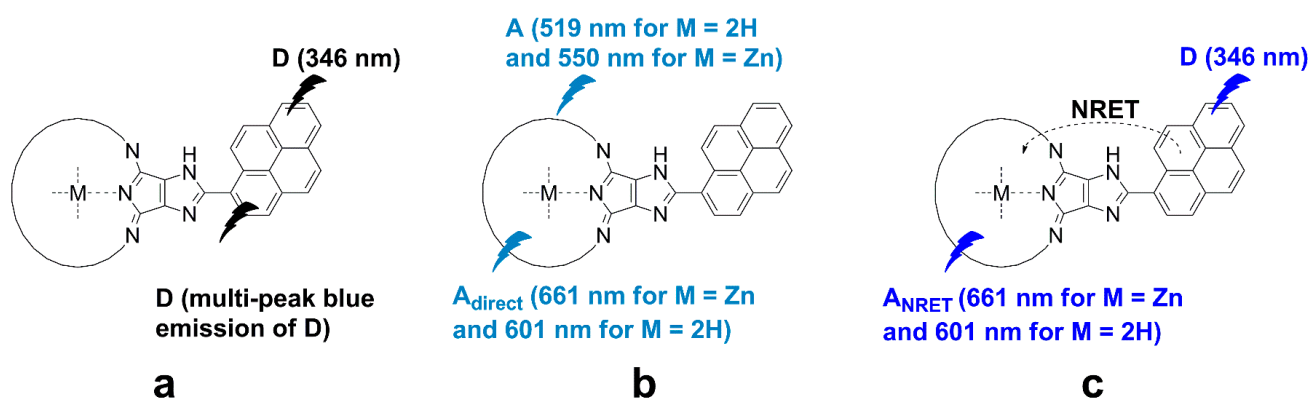


**Figure 3.** The schematic of the photophysical processes occurring in the studied dyads upon photoexcitation: (a) excitation of pyrenyl fragment and measurement of its proper emission, denoted D-D; (b) excitation of the porphyrin and measurement of its proper emission, denoted A-A<sub>direct</sub>, and (c) excitation of the pyrenyl fragment and measurement of porphyrin core emission, denoted D-A<sub>NRET</sub>.

In general, all these factors can be quantified by measuring three different fluorescence intensity values: one for the pyrene moiety and two for the porphyrin fragment (upon its direct excitation and excitation via NRET). Therefore, the ratio between the value of the pyrene fluorescence intensity and the values of any of the mentioned porphyrin emission intensities can serve as ratiometric signals on the NAC presence. Nitrobenzene (NB) and picric acid (trinitrophenol, TNP) were chosen as archetypal NAC analytes.

### 3.1. Effect of Nitrobenzene and Picric Acid on H<sub>2</sub>PIP

We first have examined the response of the studied dyads to the presence of specific analytes by UV-vis and fluorescence titration.

The first NAC that we have investigated was nitrobenzene (NB). One can see (Figure 4a) that NB addition to the dyad does not lead to any changes in the absorbance spectra of the solution (except for the obvious appearance of NB absorbance band itself). At the same time, the presence of NB drastically affects the H<sub>2</sub>PIP fluorescence spectra (Figure 4b,c). The D fluorescence intensity does not decrease gradually with the addition of NB, as expected. On the contrary, pyrene emission profile remains more or less the same, while emission maximum is significantly changed to 466 nm, as a new broad band grows at this wavelength upon NB addition. At the same time, the porphyrin core fluorescence bands (661 and 720 bands) remain unchanged upon NB addition. Notably, such lack of change is observed upon direct excitation of the porphyrin ( $\lambda_{\text{ex}} = 519 \text{ nm}$ , Figure 4b) and its excitation through the D pyrene moiety (Figure 4c).

In this case, for a calibration plot (Figure 4d), based on what we saw in Figure 4c, we have chosen the band at 466 nm to obtain the D-D value. The A-A<sub>direct</sub> and D-A<sub>NRET</sub> values using the 661 nm band emission are also depicted on the calibration plot.

For the claimed ratiometric purposes, we introduce a reciprocal coefficient that is to eliminate any errors associated with changes in the receptor dyads concentrations and extract changes caused by their interaction with NAC in tests. To do this, we have chosen a D/A<sub>NRET</sub> value—the ratio between the D-D and D-A<sub>NRET</sub> values. By doing so, we hope that this ratio, being sensitive to the D energy redistribution as a result of interaction with NAC, will represent the pure ratiometric signal lacking any artefacts. Therefore, the ratiometric D/A<sub>NRET</sub> is to be used in plotting the sensor response to the analyte in both normal and ratiometric modalities.

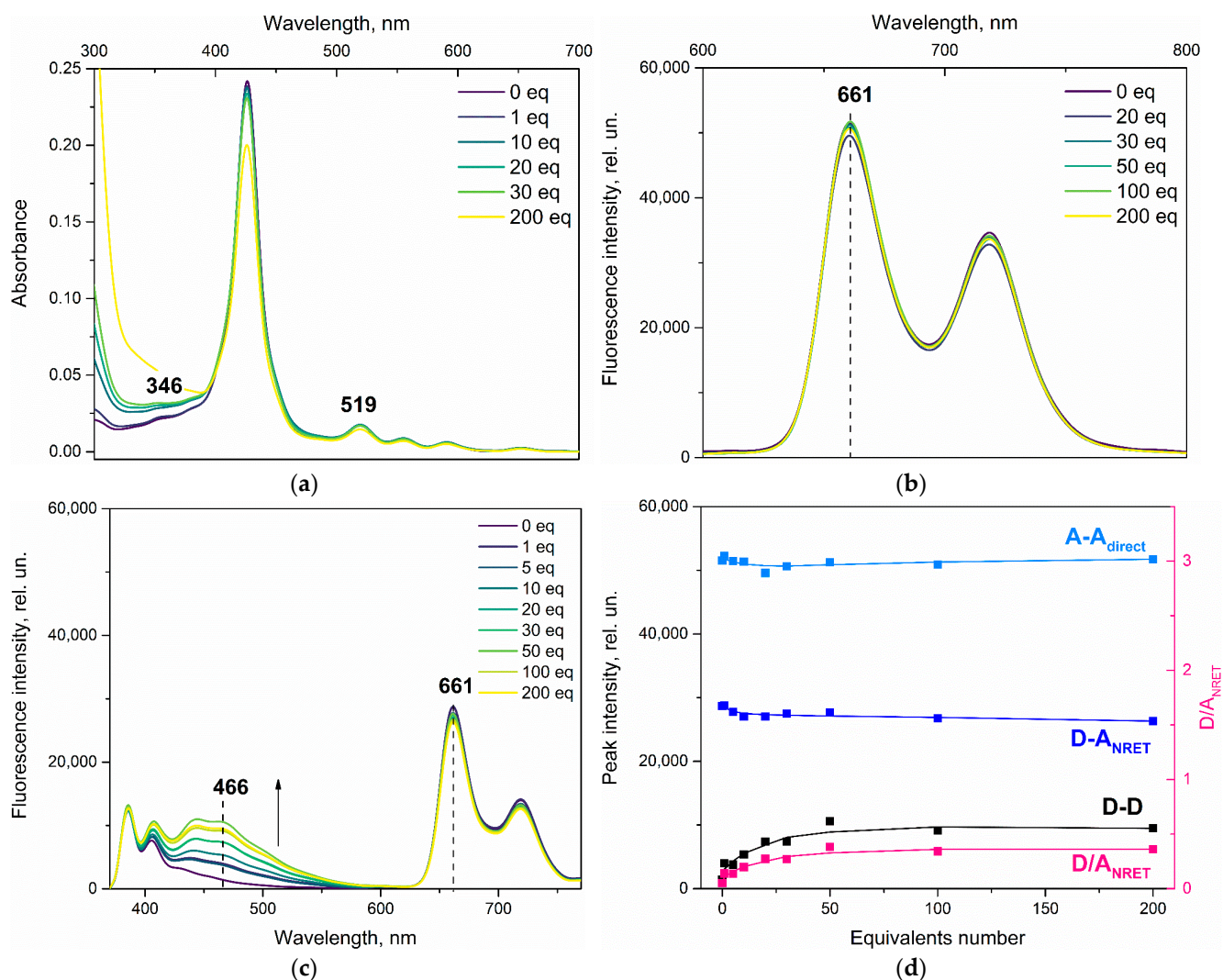


**Figure 4.** The (a) UV-vis and (b–c) fluorescence titration of H<sub>2</sub>PIP ( $7.7 \times 10^{-7}$  M) with NB (0–200 eq) in toluene upon excitation with wavelength of (b)  $\lambda_{\text{ex}} = 519$  nm (c)  $\lambda_{\text{ex}} = 346$  nm; (d) The calibration plot for H<sub>2</sub>PIP response to NB: D-D curve for the intrinsic D emission under  $\lambda_{\text{ex}} = 346$  nm, A-A<sub>direct</sub> curve for the intrinsic A emission under  $\lambda_{\text{ex}} = 519$  nm, D-A<sub>NRET</sub> curve for the A emission under  $\lambda_{\text{ex}} = 346$  nm, D/A<sub>NRET</sub> curve for the ratio between D-D and D-A<sub>NRET</sub> curves.

The obtained plot clearly depicts that the A moiety fluorescence remains almost unchanged upon addition of NB being excited via both potential NRET (D-A<sub>NRET</sub>) and direct absorbance of the light (A-A<sub>direct</sub>), while the D moiety emission intensity increases (D-D). To note, the black curve in Figure 4d corresponding to the behavior of the emission peak at 466 nm upon titration shows its maximum value at 50 equivalents of NB added and then seemingly reaches a plateau.

Doubtless, the pyrene fluorescence is not quenched by NB, but increases instead. This peculiar behavior of the H<sub>2</sub>PIP dyad will be discussed later. In this stage of the research, we wanted to investigate if this behavior was unique to NB or it could be observed for other nitroaromatic compounds.

Therefore, in the next step, in order to check the affinity of H<sub>2</sub>PIP to another member of the NAC group, we have replaced NB with picric acid (TNP). TNP, being a relatively strong acid, protonates the free-base porphyrin core quite easily. Therefore, under the TNP exposure, H<sub>2</sub>PIP demonstrates (Figure 5) the typical hyperporphyrin effect [81,82]. The shift of the Soret band to the long-wavelength region leads to a significant change in the photophysics of the porphyrin fragment [83]. The propensity of H<sub>2</sub>PIP to interact with

acids will complicate the ratiometric estimation of the NAC, resulting in the distortion of fluorescence spectra shape, which is undesirable from the standpoint of a reliable chemosensor response.

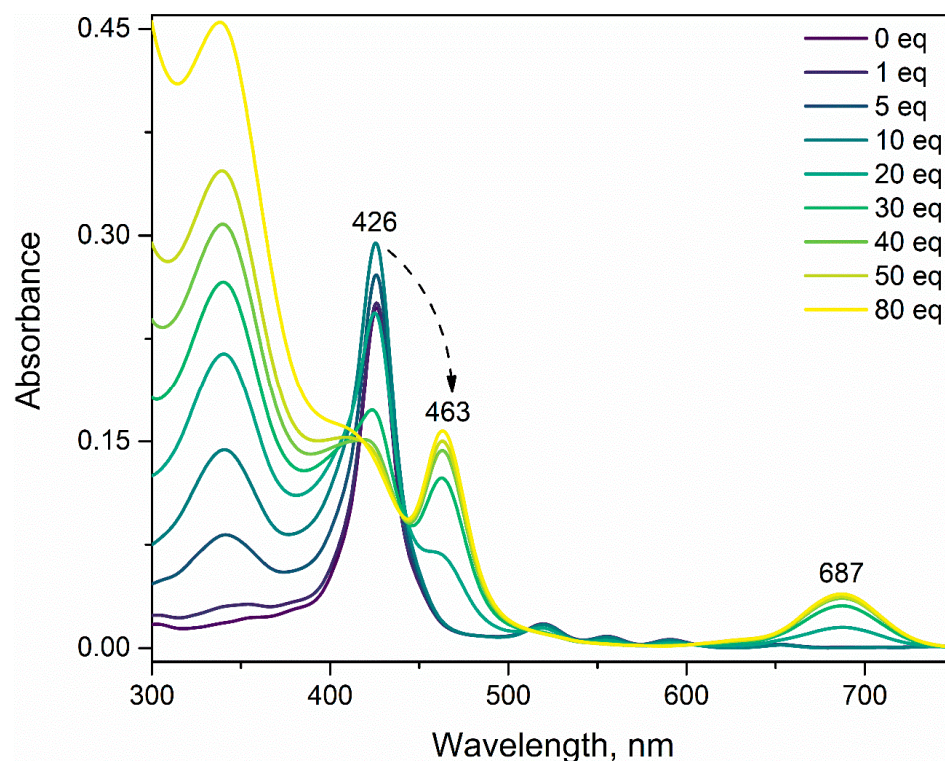


**Figure 5.** The UV-vis titration of  $\text{H}_2\text{PIP}$  ( $9.2 \times 10^{-7}$  M) with TNP (0–80 eq) in toluene. The arrow shows the shift of the Soret band upon titration.

### 3.2. Effect of Nitrobenzene on $\text{ZnPIP}$

To eliminate the dyad protonation problem, a new  $\text{ZnPIP}$  dyad has been synthesized, in which the porphyrin core contains zinc.

For comparison with the previous compound, we returned to **NB** titration, and the effect of **NB** on  $\text{ZnPIP}$  in toluene was investigated. Once more, there are no new bands and shifts in the  $\text{ZnPIP}$  absorbance spectra upon the UV-vis titration except for intrinsic **NB** absorbance in the UV region (Figure S4). One can see that the pyrene fluorescence intensity in the range of 443–550 nm (Figure 6a) also intensifies in this case upon addition of the **NB** quantity to the cuvette. The observed spectral evolution is comparable to the case of **NB**-titration of  $\text{H}_2\text{PIP}$ . Moreover, it is much more significant now and can be visible to the naked-eye (Figure 7). The calibration plot curves behave in a similar manner as well (Figure 6b). The **D-D** curve (the pyrene emission band at 459 nm in this case) tends to grow, the **D-A<sub>NRET</sub>** and **A-A<sub>direct</sub>** (the porphyrin emission band at 601 nm) also evolve in the same fashion upon **NB** addition. The **D/A<sub>NRET</sub>** curve follows the **D-D** curve shape by correlating it with the reference signal from the A moiety. Herein, it is obvious that the presence of NAC, such as **NB**, leads to  $\text{ZnPIP}$  response that is analogous to the case of  $\text{H}_2\text{PIP}$ . The only difference is the absence of the plateau on the **D-D** curve. For this case, an estimated association constant turns out to be  $2.9 \times 10^4 \text{ M}^{-1}$  (Figure S5a).

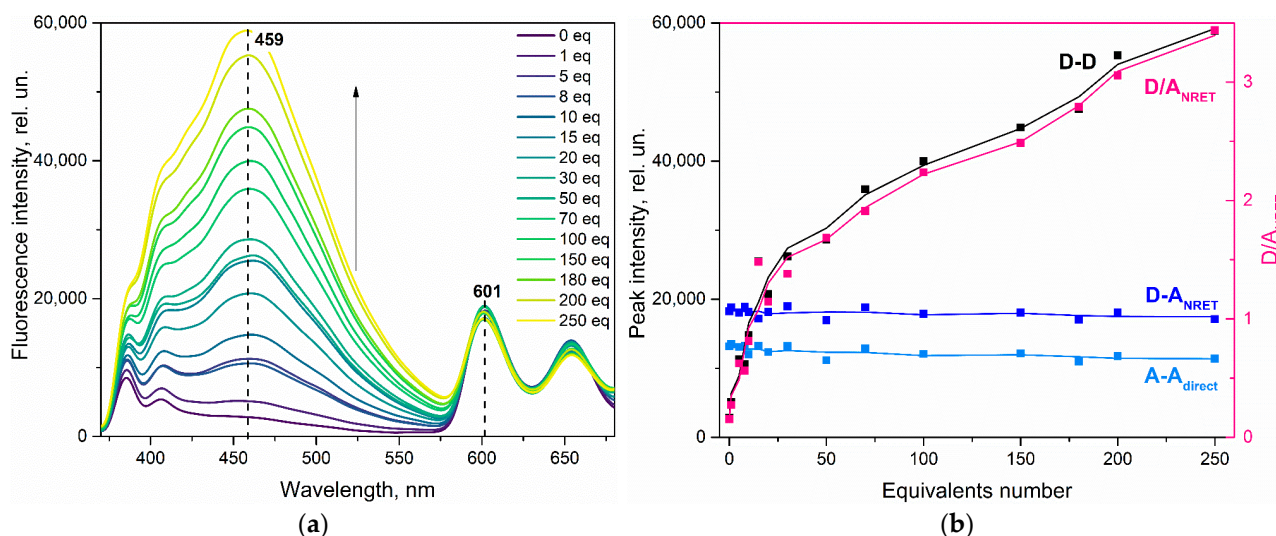


**Figure 6.** (a) The fluorescence titration of **ZnPIP** ( $7.3 \times 10^{-7}$  M) with **NB** (0–250 eq) in toluene ( $\lambda_{\text{ex}} = 346$  nm). (b) The calibration plot for **ZnPIP** response to **NB**: **D-D** curve for the intrinsic **D** emission under  $\lambda_{\text{ex}} = 346$  nm, **A-A<sub>direct</sub>** for the intrinsic **A** emission under  $\lambda_{\text{ex}} = 550$  nm, **D-A<sub>NRET</sub>** for the **A** emission under  $\lambda_{\text{ex}} = 346$  nm, **D/A<sub>NRET</sub>** for the ratio between **D-D** and **D-A<sub>NRET</sub>** curves.



**Figure 7.** The photo demonstrating visible changes of **ZnPIP** ( $7.3 \times 10^{-7}$  M) solution emission colour (under the UV light of 350 nm) before and after addition of 250 eq of **NB**.

### 3.3. Effect of Picric Acid on **ZnPIP**

Predictably, the interaction with **TNP** does not result in any redshift of the Soret band in the absorbance spectra of **ZnPIP** (Figure S6). Now that the macrocycle core protonation is eliminated, the reliable ratiometric response in the case of **TNP** detection is now feasible (Figures 8 and S2). It is apparent from these figures that the **ZnPIP** response to **TNP** is much the same as for **NB**. In the calibration plot in Figure 8b, the **D-D** curve is plotted for the pyrene emission band at 465 nm, the **D-A<sub>NRET</sub>** and **A-A<sub>direct</sub>** curves are for the porphyrin emission band at 601 nm. The association constant for this case is estimated as  $7.5 \times 10^4 \text{ M}^{-1}$  (Figure S5b).

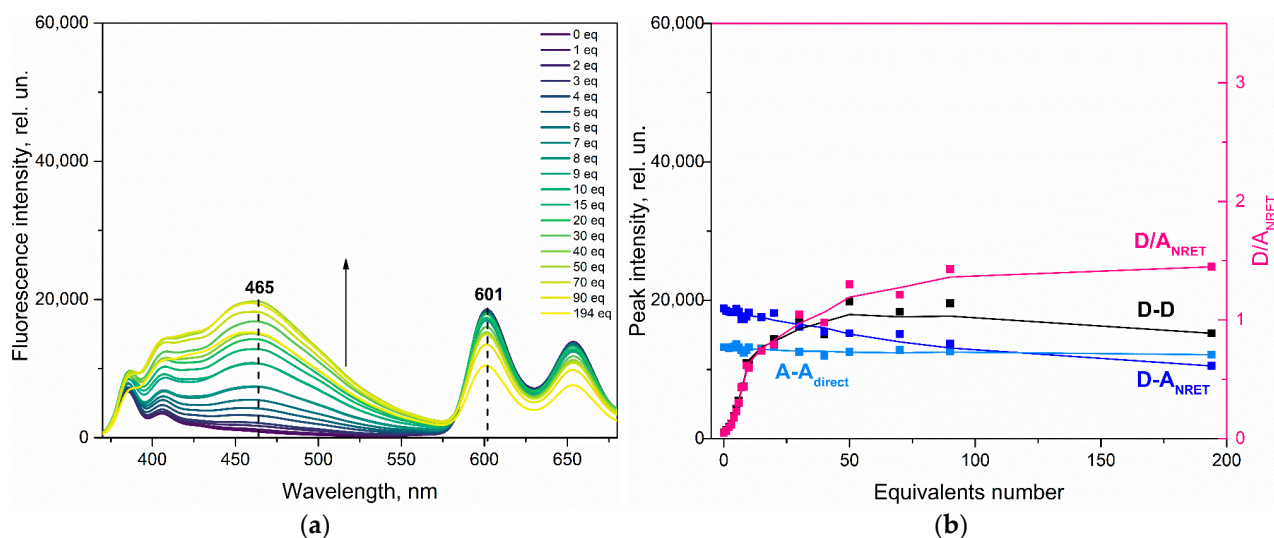


**Figure 8.** (a) The fluorescence titration of **ZnPIP** ( $7.9 \times 10^{-7}$  M) with **TNP** (0–194 eq) in toluene ( $\lambda_{\text{ex}} = 346$  nm). (b) The calibration plot for **ZnPIP** response to **NB**: **D-D** curve for the intrinsic **D** emission under  $\lambda_{\text{ex}} = 346$  nm, **A-A<sub>direct</sub>** for the intrinsic **A** emission under  $\lambda_{\text{ex}} = 550$  nm, **D-A<sub>NRET</sub>** for the **A** emission under  $\lambda_{\text{ex}} = 346$  nm, **D/A<sub>NRET</sub>** for the ratio between **D-D** and **D-A<sub>NRET</sub>** curves.

In total, it can be deduced from the calibration plots for both **H<sub>2</sub>PIP** and **ZnPIP** that the porphyrin moiety is barely affected by the NAC in all the cases above. Compared to the **D** moiety behavior, the **A** intensity dependence on the NAC amount exhibits just only slightly changing lines with no visible extremum points. The small decrease in the emission intensity of **A** upon **D** excitation in the last case can be explained by the significant absorbance of **TNP** at 346 nm (Figure S6). Therefore, one can assume that the NRET from **D** to **A** is absent or is not the main pyrene relaxation pathway. Nonetheless, due to the independent behavior of the **A** moiety, the ratiometric fluorescence assay remains valid. It is still interesting, however, that the pyrene moiety calibration curves reveal a significant increase in fluorescence upon the NAC addition.

### 3.4. Possible Causes of the **D** Fluorescence Intensity Enhancement

Observing such an atypical behavior of the dyads, we have aimed to elucidate what else can bring about the appearance of a new intense band of the **D** fluorescence.

Bearing in mind that requirements for NRET are fulfilled (such as the spectral overlap, distances between porphyrin and pyrene units, and the non-perpendicular mutual orientation of their transition dipole moments), we have assumed that the mentioned band emerged from pyrene moiety reorientation relatively to the porphyrin macrocycle.

If so, considering that the distances between **D** and **A** within the dyad molecule have not changed and the Soret band does not undergo red or blue shifts, the reorientation of the pyrenyl moiety can increase **D** emission as an outcome of NRET inhibition.

If NRET does not take place, then the initial low intensity of **D** fluorescence (Figure S8) can be due to the energy dissipation through some non-radiative relaxation. Intramolecular rotation can be one of such relaxation pathways. In turn, the restriction of this rotation on account of the interaction with NAC would lead to the **D** emission enhancement. If this is the case, the decrease of the intramolecular rotation rate in a high-viscosity environment, which can suppress the fast movement of **D**, should also restrict the rotation relaxation pathway and, consequently, enhance the **D** fluorescence [84–86].

Assuming that a viscous environment could block or slow down the pyrene fragment rotation, we have examined the **ZnPIP** behavior in 1-octanol, expecting the **D** fluorescence to enhance in the same manner as upon the NAC addition. Figure 9 shows that under the excitation at 346 nm, the **D** emission has generally intensified when dissolved in 1-octanol

in comparison with the toluene solution, whilst the **A** moiety fluorescence intensity has almost not changed.

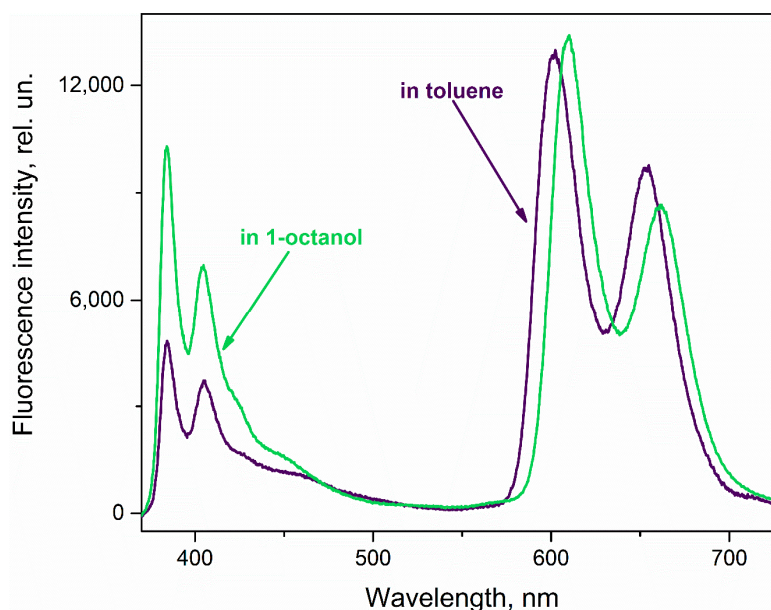


**Figure 9.** The fluorescence spectra of ZnPIP solutions ( $9.0 \times 10^{-7}$  M) in toluene and 1-octanol ( $\lambda_{\text{ex}} = 346$  nm).

Here, it is worth noting again that the **A** fluorescence in 1-octanol is almost the same as in toluene. This confirms that the excited **D** energy does not transfer to the **A** ground state (even though the spectral overlap between the **A** absorbance and **D** fluorescence becomes greater). Such observation signifies that NRET indeed does not happen in the system.

Notably, the **D** fluorescence intensity has increased even further when we immobilized ZnPIP in a poly(methyl methacrylate) (PMMA) matrix, further limiting the energy dissipation through molecular motion, particularly the rotation of the **D** fragment (Figure S9).

Analyzing these data, we can assume that the highly viscous environment indeed limits the **D** rotational relaxation pathway. This limitation, in turn, leads to an increase in the overall **D** luminescence, as the energy dissipated in a non-radiative way before is now released as the light emission. However, the intensity enhancement is not accompanied by the new **D** emission band in the region of 460–500 nm, indicating the necessary but not sufficient role of intramolecular rotation restriction in its appearance in the fluorescence titration with NAC.

It is worth noting that the addition of hexafluorobenzene, which is aromatic and can electrostatically interact with the pyrene moiety owing to its electron-deficient ring, did not give rise to the **D** emission enhancement (Figure S10). This finding may also indirectly confirm that the observed **D** emission increase may be an outcome of the pyrene fragment reorientation, not its direct interaction with an analyte.

The wide emission band appearing upon the interaction of the dyads with NAC resembles the bands observed in the fluorescence spectra of pyrene dimers (excimers) or pyrene complexes assembled with different molecules (exciplexes) [87–90]. In our case, the formation of excimers by receptor aggregation is unlikely due to the low concentration of samples; moreover, UV-vis spectra show no evidence of aggregation in the porphyrin part of the spectrum. As for exciplexes, they are usually observed when pyrene interacts with electron-rich molecules, such as anilines, nucleobases, etc. On the contrary, the interaction of NAC with pyrene derivatives does not typically cause the exciplex emission but leads to quenching of the pyrene fluorescence, as stated above. This quenching usually occurs by transferring electrons from the excited state of pyrene to NAC due to the higher LUMO energy of the electron-rich pyrene compared to the LUMO of electron-deficient NAC molecules [46,91].

Thus, neither the excimer nor the exciplex hypothesis can fully explain the appearance of the new emission band, however, we found an interesting report on the photophysics of pyrenylurea-nitrobenzene  $\pi$ -stacked protophanes [92]. These compounds contain terminal units of pyrene and nitrobenzene separated by one, two, or three phenylenediamine-based urea bridges. Depending on the length of bridges, the compounds had different fluorescence spectra, with an intense broad band at 540 nm observed in the case of the molecule with three bridges, while this band was not observed in the case of other protophanes. Femtosecond pump-probe spectroscopy combined with semiempirical ZINDO orbital calculations suggested that the photophysics of these compounds depends on the direction of charge transfer between the pyrene and either nitrobenzene or phenylenediamine units. Thus, the inspection of the orbital structure of photoactive receptor complexes with NAC may provide the first clues to explaining their anomalous spectral properties.

We performed geometric optimization of the **ZnPIP** molecule and its supramolecular complex with nitrobenzene (Figure 10). Optimization was performed using  $r^2$ SCAN-3c “Swiss army knife” composite electronic-structure method, affording accurate geometries of both covalent and noncovalent systems [63]. Solvation effects in toluene media were accounted within CPCM model [64]. The obtained geometries were analyzed to visualize and identify the intermolecular noncovalent interactions (NCI) in terms of reduced density gradient (RDG) analysis [93]:

$$\text{RDG}(\mathbf{r}) = \frac{1}{2(3\pi^2)^{2/3}} \cdot \frac{[\Delta\rho(\mathbf{r})]}{[\rho(\mathbf{r})]^{4/3}} \quad (1)$$

Here,  $\rho$  is the electron density, and  $\mathbf{r}$  is the coordinate vector. The isosurface map of the RDG in the low electron density region gives a visual representation (in the upper left corner of Figure 10) of noncovalent interactions, where the regions of weaker Van der Waals interactions are colored green, while stronger attraction and repulsion are colored blue and red, respectively. According to the NCI-RDG method, the type and strength of interaction can be determined by the  $\text{sign}(\lambda_2)\rho$ , where the  $\text{sign}(\lambda_2)\rho$  is the sign of the second highest eigenvalue of the Hessian electron density matrix at position  $\mathbf{r}$ . Thus, the  $\text{sign}(\lambda_2)\rho$  value will be negative for attractive interactions and positive for repulsive ones. Further integration the NCI-RDG results with the Quantum theory of atoms in molecules made it possible to identify interacting atoms because they are connected by bonding paths that cross NCI isosurfaces at critical points (3,−1).

The pristine receptor has a twist of 27.8° between imidazoporphyrin and pyrenyl units, the conformation is stabilized by the balance of attractive interactions of pyrenyl moiety with meso-aryl substituents and repulsion between CH and NH groups.

The twist angle increases to 42.1° upon binding of nitrobenzene. This binding occurs mainly due to stacking interactions with pyrene unit with some contributions from  $\text{NO}_2 \cdots \pi$  interactions with one of the meso-aryl substituents as well as hydrogen bonding between the oxygen atom of  $\text{NO}_2$ -group and imidazolyl NH-group. The distance between centroids of nitrobenzene and pyrenyl group has a value of 3.44 Å, which is close to doubled van der Waals radius of carbon.

Further analysis of the electronic structure of **ZnPIP** and its complex with nitrobenzene was performed using the CAM-B3LYP/6-31G(d) wavefunctions obtained for the optimized geometries (Figure 11). Inspection of localization of frontier orbitals on certain fragments of molecules evidenced that in pristine receptor  $\pi$ -systems of pyrenyl and imidazoporphyrin units are essentially localized. It is important to note that on the energy scale, the block of porphyrin-centered Gouterman orbitals is located between the orbitals localized on the pyrene fragment. Thus, excitation of the latter fragment can result in energy transfer to the porphyrin, resulting in dual fluorescence of the dyad.

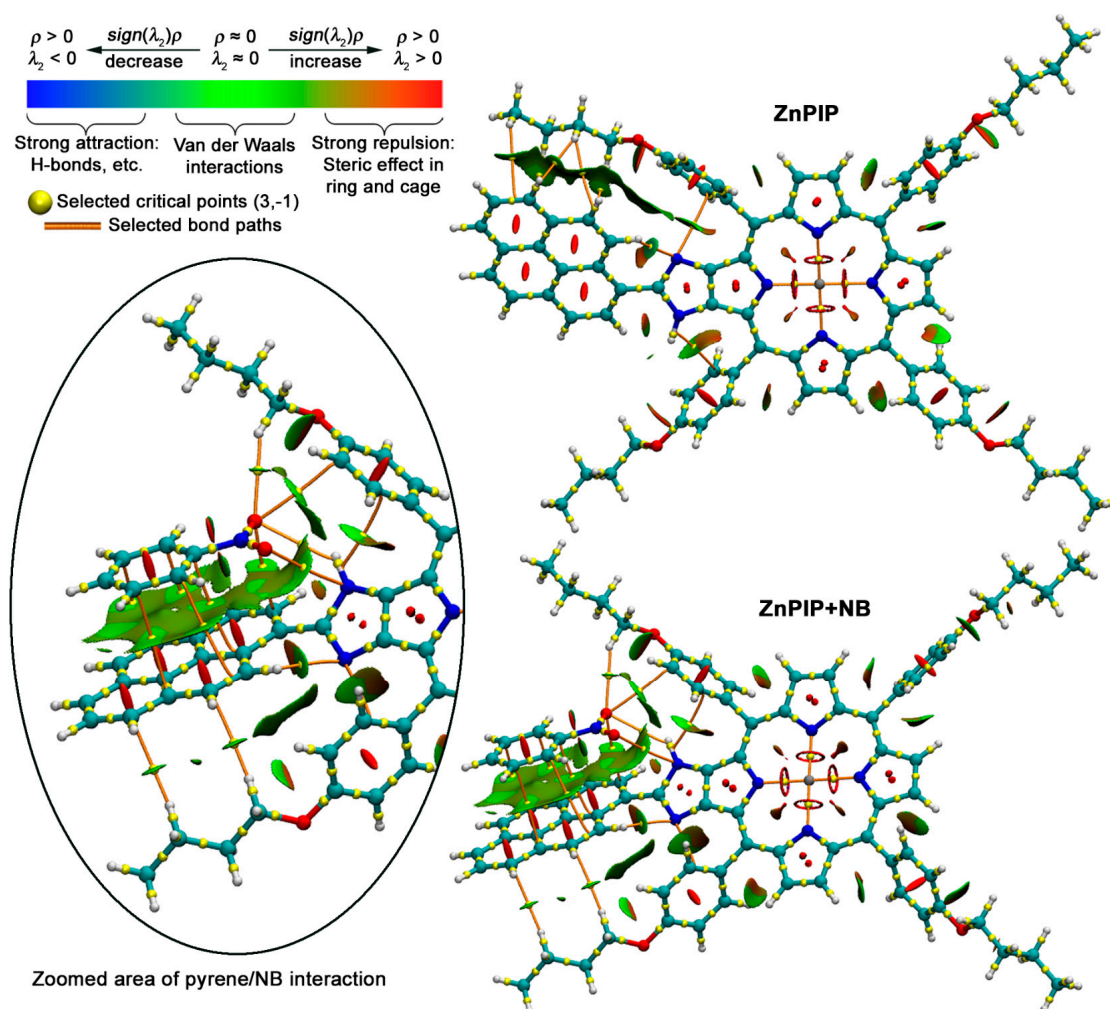


**Figure 10.** NCI plots for ZnPIP and ZnPIP+NB molecules with critical points (3,−1) and bond paths indicating noncovalent interactions. The inset in top left corner shows the qualitative dependence of the isosurface colour on the strength of the noncovalent interaction, with some examples of corresponding interactions listed. Geometries were optimized at r<sup>2</sup>SCAN-3c level of theory using CPCM solvation model for toluene media.

Once nitrobenzene interacts with the receptor, porphyrin LUMO becomes delocalized—it forms bonding and antibonding combinations nitrobenzene LUMO, thus relaxation of the excited state of the excited pyrene moiety might proceed via a more complicated pathway rather than simple electron transfer to nitrobenzene, which was observed previously in less sophisticated sensing systems [44,85].

For sure, it is early to draw some definitive conclusions concerning the influence of such a peculiar electronic structure on the unusual spectral response of ZnPIP to nitrobenzene, and more experiments, especially time-resolved methods are required. The results of such ongoing measurements will be reported elsewhere.

Nevertheless, we emphasize that the disclosed phenomenon of fluorescence enhancement is not an obstacle to the ratiometric estimation of the NAC presence. It has turned out that the dual emission of the dyad consisted of one changeable signal (the **D** emission) sensitive to the analyte and one permanent signal (the **A** emission) serving as a reference signal itself. Thus, in fact, the reported dyad can be regarded as the ratiometric ‘turn-on’ receptor with two mutually independent fluorophores.

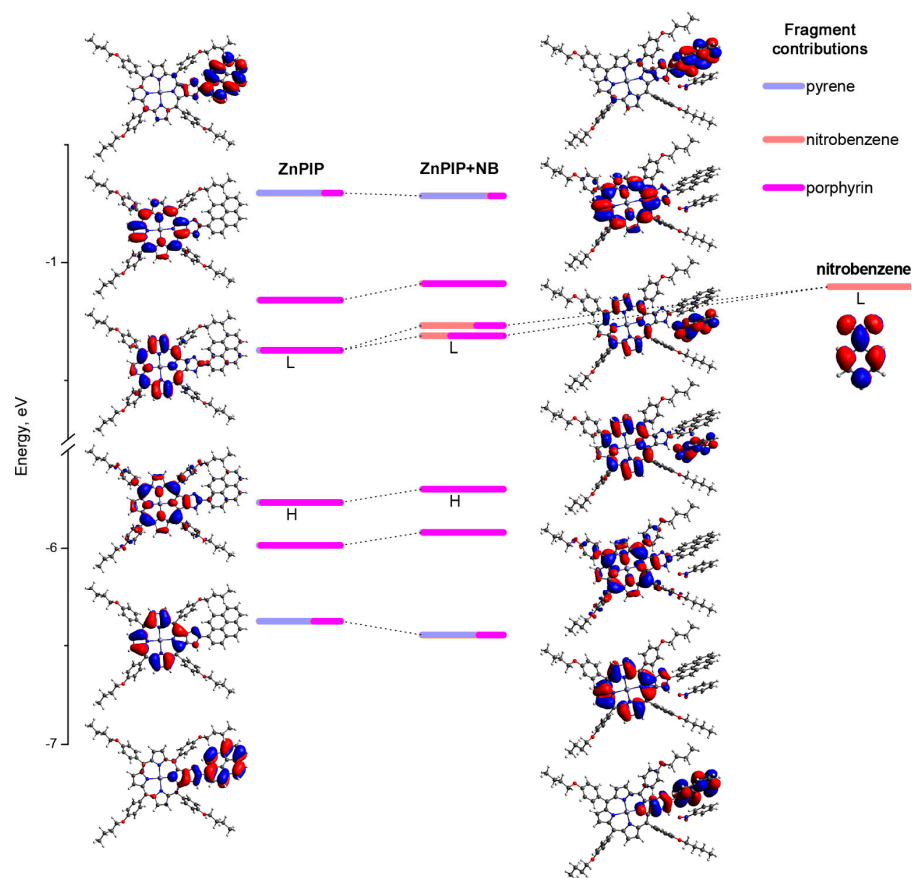


**Figure 11.** Diagram of frontier orbitals of **ZnPIP**, **ZnPIP+NB** and nitrobenzene. Energies and symmetries of orbitals were calculated at CAM-B3LYP/6-31G(d)+CPCM(toluene) level of theory for r<sup>2</sup>SCAN-3c optimized geometries. The bars, corresponding to positions of certain orbitals on the energy scale, show the partitioning of orbitals between imidazoporphyrin, pyrene and nitrobenzene fragments.

#### 4. Conclusions

In the present study, the atypical behavior of the ratiometric dyads (**H<sub>2</sub>PIP** and **ZnPIP**) consisting of two fluorophores that, at a first glance, should be capable of NRET and suitable for the ‘turn-off’ NAC sensors modelling has been revealed.

We have found that the addition of nitroaromatic compounds to any of these dyads did not reduce, but instead significantly increased the intensity of the donor fragment fluorescence. It has been shown that the low initial intensity of the pyrenyl fragment emission, firstly misconstrued as NRET, could be a consequence of the intramolecular rotational relaxation and any restriction of such rotation could cause the **D** fluorescence enhancement. As evidence, the quantum chemical calculations have verified the possibility of reorientation of the dyad compartments leading to the pyrenyl group twist generated by the interaction with the NAC molecule. Presumably, this interplay induces **D** fluorescence amplification, blocking the rotational movements of the latter. Additionally, due to these calculations, we conclude that the observed photophysical outcome is something more complex than one particular relaxation pathway of the excited state of the dyad.

The discovered phenomenon is of great interest since examples of ‘turn-on’ sensors for NAC are quite rare. Moreover, apart from the turn-on response of **D**, the studied compound also exhibits stable porphyrin emission that is independent from analyte concentration. The presence of two fluorescence signals enables a ratiometric analytical approach. Additionally, from a broader perspective, the effect of the pyrene emission enhancement in the dyads of such type could find its application in the molecular viscosity sensors.

**Supplementary Materials:** The following supporting information can be downloaded at: <https://www.mdpi.com/article/10.3390/chemosensors11010043/s1>, Figure S1: The UV-vis spectra of **NB** ( $7.8 \times 10^{-4}$  M) and **TNP** ( $7.1 \times 10^{-4}$  M) solutions in toluene; Figure S2: The fluorescence spectrum of toluene solution of **H<sub>2</sub>PIP** ( $7.6 \times 10^{-7}$  M) before correction (the black curve) and after correction (the blue curve) by the subtraction of the toluene background with Rayleigh scattering and the 2<sup>nd</sup> order diffraction artefact from the 346 nm excitation light; Figure S3: The UV-vis absorbance and fluorescence spectra of **TPP** ( $5.8 \times 10^{-7}$  M) solution in toluene [72]; Figure S4: The UV-vis titration of **ZnPIP** solution ( $7.3 \times 10^{-7}$  M) with **NB** (0–250 eq) in toluene; Figure S5: The  $K_a$  calculation plot for **ZnPIP** under (a) **NB** addition and (b) **TNP** addition [94]; Figure S6: The UV-vis titration of **ZnPIP** solution ( $7.9 \times 10^{-7}$  M) with **TNP** (0–194 eq) in toluene; Figure S7: The fluorescence titration of **ZnPIP** ( $7.9 \times 10^{-7}$  M) with **TNP** (0–194 eq) under the direct A excitation (550 nm) in toluene; Figure S8: The comparison of **BIP** ( $8.0 \times 10^{-7}$  M) and **ZnPIP** ( $7.6 \times 10^{-7}$  M) solutions in toluene fluorescence spectra toluene ( $\lambda_{ex} = 346$  nm) under the same experimental conditions. In the inset: the zoomed **ZnPIP** spectrum; Figure S9: The fluorescence (the green curve) and UV-vis absorbance (the black curve) spectra of ‘**ZnPIP** in **PMMA**’ solid film under 346 nm excitation; Figure S10: The UV-Vis and fluorescence ( $\lambda_{ex} = 346$  nm) titration of **ZnPIP** solution ( $7.5 \times 10^{-7}$  M) with **C<sub>6</sub>F<sub>6</sub>** in toluene.

**Author Contributions:** Conceptualization, A.V.S., S.L.S. and Y.G.G.; formal analysis, I.I.S.; funding acquisition, A.Y.T. and Y.G.G.; investigation, I.I.S. and A.G.M.; methodology, I.I.S., A.V.S. and S.L.S.; project administration, A.Y.T. and Y.G.G.; resources, K.P.B., D.A.P. and Y.G.G.; supervision, Y.G.G.; validation, I.I.S.; visualization, I.I.S. and A.G.M.; writing—original draft, I.I.S.; writing—review and editing, A.G.M., A.V.S. and S.L.S. All authors have read and agreed to the published version of the manuscript.

**Funding:** The work was supported by the Ministry of Science and Higher Education of Russia (grant agreement no. 075-15-2020-782).

**Institutional Review Board Statement:** Not applicable.

**Informed Consent Statement:** Not applicable.

**Data Availability Statement:** Not applicable.

**Conflicts of Interest:** The authors declare no conflict of interest.

## References

1. Kovacic, P.; Somanathan, R. Nitroaromatic Compounds: Environmental Toxicity, Carcinogenicity, Mutagenicity, Therapy and Mechanism. *J. Appl. Toxicol.* **2014**, *34*, 810–824. [[CrossRef](#)] [[PubMed](#)]
2. Ju, K.-S.; Parales, R.E. Nitroaromatic Compounds, from Synthesis to Biodegradation. *Microbiol. Mol. Biol. Rev.* **2010**, *74*, 250–272. [[CrossRef](#)] [[PubMed](#)]
3. Akhavan, J. *The Chemistry of Explosives*; Royal Society of Chemistry: London, UK, 2011; p. 4. ISBN 978-1-84973-330-4.
4. Spain, J.C. Biodegradation of Nitroaromatic Compounds. *Annu. Rev. Microbiol.* **1995**, *49*, 523–555. [[CrossRef](#)] [[PubMed](#)]
5. Kulkarni, M.; Chaudhari, A. Microbial Remediation of Nitro-Aromatic Compounds: An Overview. *J. Environ. Manag.* **2007**, *85*, 496–512. [[CrossRef](#)]
6. Boelsterli, U.; Ho, H.; Zhou, S.; Yeow Leow, K. Bioactivation and Hepatotoxicity of Nitroaromatic Drugs. *Curr. Drug Metab.* **2006**, *7*, 715–727. [[CrossRef](#)] [[PubMed](#)]
7. Miliukiene, V.; Čenas, N. Cytotoxicity of Nitroaromatic Explosives and Their Biodegradation Products in Mice Splenocytes: Implications for Their Immunotoxicity. *Z. Fur Nat. Sect. C J. Biosci.* **2008**, *63*, 519–525. [[CrossRef](#)] [[PubMed](#)]
8. Zyryanov, G.V.; Kopchuk, D.S.; Kovalev, I.S.; Nosova, E.V.; Rusinov, V.L.; Chupakhin, O.N. Chemosensors for Detection of Nitroaromatic Compounds (Explosives). *Russ. Chem. Rev.* **2014**, *83*, 783. [[CrossRef](#)]
9. Giannoukos, S.; Brkić, B.; Taylor, S.; Marshall, A.; Verbeck, G.F. Chemical Sniffing Instrumentation for Security Applications. *Chem. Rev.* **2016**, *116*, 8146–8172. [[CrossRef](#)]
10. Akhgari, F.; Fattahi, H.; Oskoei, Y.M. Recent Advances in Nanomaterial-Based Sensors for Detection of Trace Nitroaromatic Explosives. *Sens. Actuators B Chem.* **2015**, *221*, 867–878. [[CrossRef](#)]
11. Sylvia, J.M.; Janni, J.A.; Klein, J.D.; Spencer, K.M. Surface-Enhanced Raman Detection of 2,4-Dinitrotoluene Impurity Vapor as a Marker to Locate Landmines. *Anal. Chem.* **2000**, *72*, 5834–5840. [[CrossRef](#)]
12. Stahl, D.C.; Tilotta, D.C. Screening Method for Nitroaromatic Compounds in Water Based on Solid-Phase Microextraction and Infrared Spectroscopy. *Environ. Sci. Technol.* **2001**, *35*, 3507–3512. [[CrossRef](#)] [[PubMed](#)]
13. Walsh, M.E. Determination of Nitroaromatic, Nitramine, and Nitrate Ester Explosives in Soil by Gas Chromatography and an Electron Capture Detector. *Talanta* **2001**, *54*, 427–438. [[CrossRef](#)] [[PubMed](#)]
14. Moore, D.S. Instrumentation for Trace Detection of High Explosives. *Rev. Sci. Instrum.* **2004**, *75*, 2499–2512. [[CrossRef](#)]

15. Wong, M.H.; Giraldo, J.P.; Kwak, S.-Y.; Koman, V.B.; Sinclair, R.; Lew, T.T.S.; Bisker, G.; Liu, P.; Strano, M.S. Nitroaromatic Detection and Infrared Communication from Wild-Type Plants Using Plant Nanobionics. *Nat. Mater.* **2016**, *16*, 264–272. [[CrossRef](#)]
16. Verbitskiy, E.V.; Rusinov, G.L.; Chupakhin, O.N.; Charushin, V.N. Design of Fluorescent Sensors Based on Azaheterocyclic Push-Pull Systems towards Nitroaromatic Explosives and Related Compounds: A Review. *Dye. Pigment.* **2020**, *180*, 108414. [[CrossRef](#)]
17. Salinas, Y.; Mañez, R.M.; Marcos, M.D.; Sancenón, F.; Costero, A.M.; Parra, M.; Gil, S. Optical Chemosensors and Reagents to Detect Explosives. *Chem. Soc. Rev.* **2012**, *41*, 1261–1296. [[CrossRef](#)]
18. Vora, M.; Panchal, M.; Dey, S.; Pandya, A.; Athar, M.; Verma, N.; Irfan, A.; Jain, V.K. Oxacalix[4]Arene Based Dual-Signalling Fluorimetric and Electrochemical Chemosensor for the Selective Detection of Nitroaromatic Compounds. *J. Mol. Liq.* **2022**, *362*, 119791. [[CrossRef](#)]
19. Chhatwal, M.; Mittal, R.; Gupta, R.D.; Awasthi, S.K. Sensing Ensembles for Nitroaromatics. *J. Mater. Chem. C* **2018**, *6*, 12142–12158. [[CrossRef](#)]
20. Brzechwa-Chodzyńska, A.; Drożdż, W.; Harrowfield, J.; Stefankiewicz, A.R. Fluorescent Sensors: A Bright Future for Cages. *Coord. Chem. Rev.* **2021**, *434*, 213820. [[CrossRef](#)]
21. Kalva, N.; Tran, C.H.; Lee, M.W.; Augustine, R.; Lee, S.J.; Kim, I. Aggregation-Induced Emission-Active Hyperbranched Polymers Conjugated with Tetraphenylethylene for Nitroaromatic Explosive Detection. *Dye. Pigment.* **2021**, *194*, 109617. [[CrossRef](#)]
22. Martínez-Mañez, R.; Sancenón, F. Fluorogenic and Chromogenic Chemosensors and Reagents for Anions. *Chem. Rev.* **2003**, *103*, 4419–4476. [[CrossRef](#)] [[PubMed](#)]
23. Akkoc, E.; Karagoz, B. One Step Synthesis of Crosslinked Fluorescent Microspheres for the Effective and Selective Sensing of Explosives in Aqueous Media. *Eur. Polym. J.* **2022**, *172*, 111238. [[CrossRef](#)]
24. Mauricio, F.G.M.; Silva, J.Y.R.; Talhavini, M.; Júnior, S.A.; Weber, I.T. Luminescent Sensors for Nitroaromatic Compound Detection: Investigation of Mechanism and Evaluation of Suitability of Using in Screening Test in Forensics. *Microchem. J.* **2019**, *150*, 104037. [[CrossRef](#)]
25. Lakowicz, J.R. *Principles of Fluorescence Spectroscopy*; Springer: Berlin/Heidelberg, Germany, 2006; pp. 1–954. [[CrossRef](#)]
26. Gogoi, B.; Sarma, N. Sen Curcumin–Cysteine and Curcumin–Tryptophan Conjugate as Fluorescence Turn On Sensors for Picric Acid in Aqueous Media. *ACS Appl. Mater. Interfaces* **2015**, *7*, 11195–11202. [[CrossRef](#)] [[PubMed](#)]
27. Sivaraman, G.; Vidya, B.; Chellappa, D. Rhodamine Based Selective Turn-on Sensing of Picric Acid. *RSC Adv.* **2014**, *4*, 30828–30831. [[CrossRef](#)]
28. Lee, J.Y.; Root, H.D.; Ali, R.; An, W.; Lynch, V.M.; Bähring, S.; Kim, I.S.; Sessler, J.L.; Park, J.S. Ratiometric Turn-On Fluorophore Displacement Ensembles for Nitroaromatic Explosives Detection. *J. Am. Chem. Soc.* **2020**, *142*, 19579–19587. [[CrossRef](#)]
29. Lin, Q.; Guan, X.W.; Fan, Y.Q.; Wang, J.; Liu, L.; Liu, J.; Yao, H.; Zhang, Y.M.; Wei, T.B. A Tripodal Supramolecular Sensor to Successively Detect Picric Acid and CN<sup>-</sup> through Guest Competitive Controlled AIE. *New J. Chem.* **2019**, *43*, 2030–2036. [[CrossRef](#)]
30. Xu, Y.; Li, B.; Li, W.; Zhao, J.; Sun, S.; Pang, Y. “ICT-Not-Quenching,, near Infrared Ratiometric Fluorescent Detection of Picric Acid in Aqueous Media. *Chem. Commun.* **2013**, *49*, 4764–4766. [[CrossRef](#)]
31. Li, L.; Cheng, J.; Liu, Z.; Song, L.; You, Y.; Zhou, X.; Huang, W. Ratiometric Luminescent Sensor of Picric Acid Based on the Dual-Emission Mixed-Lanthanide Coordination Polymer. *ACS Appl. Mater. Interfaces* **2018**, *10*, 44109–44115. [[CrossRef](#)]
32. Taya, P.; Maiti, B.; Kumar, V.; De, P.; Satapathi, S. Design of a Novel FRET Based Fluorescent Chemosensor and Their Application for Highly Sensitive Detection of Nitroaromatics. *Sens. Actuators B Chem.* **2018**, *255*, 2628–2634. [[CrossRef](#)]
33. Chen, X.; Ma, Y.; Chen, H.; Wang, F.; Kambam, S.; Wang, Y.; Mao, C. A Highly Sensitive and Selective Ratiometric Fluorescent Sensor for Zn<sup>2+</sup> Ion Based on ICT and FRET. *Dye. Pigment.* **2014**, *102*, 301–307. [[CrossRef](#)]
34. Wang, Y.; Yang, M.Y.; Zheng, M.H.; Zhao, X.L.; Xie, Y.Z.; Jin, J.Y. 2-Pyridylthiazole Derivative as ICT-Based Ratiometric Fluorescent Sensor for Fe(III). *Tetrahedron Lett.* **2016**, *57*, 2399–2402. [[CrossRef](#)]
35. Deore, P.S.; Coman, D.S.; Manderville, R.A. A Coumarin–Hemicyanine Hybrid as a Ratiometric Fluorescent Sensor of Microenvironment Proticity. *Chem. Commun.* **2019**, *55*, 3540–3543. [[CrossRef](#)] [[PubMed](#)]
36. Zhang, W.; Wang, H.; Li, F.; Chen, Y.; Kwok, R.T.K.; Huang, Y.; Zhang, J.; Hou, J.; Tang, B.Z. A Ratiometric Fluorescent Probe Based on AIEgen for Detecting HClO in Living Cells. *Chem. Commun.* **2020**, *56*, 14613–14616. [[CrossRef](#)] [[PubMed](#)]
37. Chen, L.; Liu, D.; Peng, J.; Du, Q.; He, H. Ratiometric Fluorescence Sensing of Metal-Organic Frameworks: Tactics and Perspectives. *Coord. Chem. Rev.* **2020**, *404*, 213113. [[CrossRef](#)]
38. Dhiman, S.; Ahmad, M.; Kumar, G.; Luxami, V.; Singh, P.; Kumar, S. Ratiometric Chemosensor for Differentiation of TNP from Other NACs Using Distinct Blue Fluorescence and Visualization of Latent Fingerprints. *J. Mater. Chem. C* **2021**, *9*, 1097–1106. [[CrossRef](#)]
39. He, L.; Dong, B.; Liu, Y.; Lin, W. Fluorescent Chemosensors Manipulated by Dual/Triple Interplaying Sensing Mechanisms. *Chem. Soc. Rev.* **2016**, *45*, 6449–6461. [[CrossRef](#)]
40. Kowanko, D.; Schuster, J.; Amecke, N.; Abdel-Mottaleb, M.; Dobrawa, R.; Würthner, F.; Von Borczyskowski, C. FRET and Ligand Related NON-FRET Processes in Single Quantum Dot-Perylene Bisimide Assemblies. *Phys. Chem. Chem. Phys.* **2010**, *12*, 4112–4123. [[CrossRef](#)]
41. Shchepinov, M.S.; Korshun, V.A.; Egeland, R.D.; Southern, E.M. Tritylisation of Pyrene, Perylene and Coronene: A New Family of Switchable Fluorescent Labels. *Tetrahedron Lett.* **2000**, *41*, 4943–4948. [[CrossRef](#)]
42. Hong, Y.; Kim, J.; Kim, W.; Kaufmann, C.; Kim, H.; Würthner, F.; Kim, D. Efficient Multiexciton State Generation in Charge-Transfer-Coupled Perylene Bisimide Dimers via Structural Control. *J. Am. Chem. Soc.* **2020**, *142*, 7845–7857. [[CrossRef](#)]

43. Karuppanan, S.; Chambron, J.-C. Supramolecular Chemical Sensors Based on Pyrene Monomer–Excimer Dual Luminescence. *Chem. Asian J.* **2011**, *6*, 964–984. [[CrossRef](#)] [[PubMed](#)]
44. Liu, X.; Zhang, N.; Zhou, J.; Chang, T.; Fang, C.; Shangguan, D. A Turn-on Fluorescent Sensor for Zinc and Cadmium Ions Based on Perylene Tetracarboxylic Diimide. *Analyst* **2013**, *138*, 901–906. [[CrossRef](#)] [[PubMed](#)]
45. Bhatta, S.R.; Mondal, B.; Vijaykumar, G.; Thakur, A. ICT–Isomerization-Induced Turn-On Fluorescence Probe with a Large Emission Shift for Mercury Ion: Application in Combinational Molecular Logic. *Inorg. Chem.* **2017**, *56*, 11577–11590. [[CrossRef](#)] [[PubMed](#)]
46. Kathiravan, A.; Gowri, A.; Khamrang, T.; Kumar, M.D.; Dhenadhayalan, N.; Lin, K.-C.; Velusamy, M.; Jaccob, M. Pyrene-Based Chemosensor for Picric Acid—Fundamentals to Smartphone Device Design. *Anal. Chem.* **2019**, *91*, 13244–13250. [[CrossRef](#)] [[PubMed](#)]
47. Reddy, K.L.; Kumar, A.M.; Dhir, A.; Krishnan, V. Selective and Sensitive Fluorescent Detection of Picric Acid by New Pyrene and Anthracene Based Copper Complexes. *J. Fluoresc.* **2016**, *26*, 2041–2046. [[CrossRef](#)]
48. Rajasekaran, P.; Kannan, H.; Das, S.; Young, M.; Santra, S. Comparative Analysis of Copper and Zinc Based Agrichemical Biocide Products: Materials Characteristics, Phytotoxicity and in Vitro Antimicrobial Efficacy. *AIMS Environ. Sci.* **2016**, *3*, 439–455. [[CrossRef](#)]
49. Sun, X.; Wang, Y.; Lei, Y. Fluorescence Based Explosive Detection: From Mechanisms to Sensory Materials. *Chem. Soc. Rev.* **2015**, *44*, 8019–8061. [[CrossRef](#)]
50. Shanmugaraju, S.; Mukherjee, P.S.  $\pi$ -Electron Rich Small Molecule Sensors for the Recognition of Nitroaromatics. *Chem. Commun.* **2015**, *51*, 16014–16032. [[CrossRef](#)]
51. Jeyasingh, V.; Murugesan, K.; Lakshminarayanan, S.; Selvapalam, N.; Das, G.; Piramuthu, L. Pyrene-Hydrazone-PI…Hole Coupled Turn-on Fluorescent and Naked-Eye Colorimetric Sensor for Cyanide: Role of Homogeneous  $\pi$ -Hole Dispersion in Anion Selectivity. *J. Fluoresc.* **2021**, *31*, 1303–1309. [[CrossRef](#)]
52. Kowser, Z.; Jin, C.C.; Jiang, X.; Rahman, S.; Georghiou, P.E.; Ni, X.L.; Zeng, X.; Redshaw, C.; Yamato, T. Fluorescent Turn-on Sensors Based on Pyrene-Containing Schiff Base Derivatives for  $\text{Cu}^{2+}$  Recognition: Spectroscopic and DFT Computational Studies. *Tetrahedron* **2016**, *72*, 4575–4581. [[CrossRef](#)]
53. Liu, Y.; Zhang, Y.; Sheng, M.; Kang, Y.; Jia, B.; Li, W.; Fu, Y. A Novel Pyrene-Based Fluorescent Probe for  $\text{Al}^{3+}$  Detection. *Spectrochim. Acta Part A Mol. Biomol. Spectrosc.* **2023**, *287*, 122085. [[CrossRef](#)]
54. Xu, Z.; Singh, N.J.; Lim, J.; Pan, J.; Kim, H.N.; Park, S.; Kim, K.S.; Yoon, J. Unique Sandwich Stacking of Pyrene-Adenine-Pyrene for Selective and Ratiometric Fluorescent Sensing of ATP at Physiological pH. *J. Am. Chem. Soc.* **2009**, *131*, 15528–15533. [[CrossRef](#)] [[PubMed](#)]
55. Yoon, S.A.; Lee, J.; Lee, M.H. A Ratiometric Fluorescent Probe for  $\text{Zn}^{2+}$  Based on Pyrene-Appended Naphthalimide-Dipicolylamine. *Sens. Actuators B Chem.* **2018**, *258*, 50–55. [[CrossRef](#)]
56. Hou, M.; Fan, L.; Fan, X.; Liang, X.; Zhang, W.; Ding, Y. Pyrene-Porphyrin Based Ratiometric Fluorescent Sensor Array for Discrimination of Glycosaminoglycans. *Anal. Chim. Acta* **2021**, *1141*, 214–220. [[CrossRef](#)] [[PubMed](#)]
57. Dai, Q.; Liu, W.; Zhuang, X.; Wu, J.; Zhang, H.; Wang, P. Ratiometric Fluorescence Sensor Based on a Pyrene Derivative and Quantification Detection of Heparin in Aqueous Solution and Serum. *Anal. Chem.* **2011**, *83*, 6559–6564. [[CrossRef](#)] [[PubMed](#)]
58. Birin, K.P.; Abdulaeva, I.A.; Polivanovskaia, D.A.; Martynov, A.G.; Shokurov, A.V.; Gorbunova, Y.G.; Tsvadze, A.Y. Imidazopyrins with Appended Polycyclic Aromatic Hydrocarbons: To Conjugate or Not to Conjugate? *Dye. Pigment.* **2021**, *186*, 109042. [[CrossRef](#)]
59. Zhao, M.; Deng, Z.; Tang, J.; Zhou, X.; Chen, Z.; Li, X.; Yang, L.; Ma, L.-J. 2-(1-Pyrenyl) Benzimidazole as a Ratiometric and “Turn-on” Fluorescent Probe for Iron(III) Ions in Aqueous Solution. *Analyst* **2016**, *141*, 2308–2312. [[CrossRef](#)]
60. Armarego, W.L. *Purification of Laboratory Chemicals*; Butterworth-Heinemann: Oxford, UK, 2017; ISBN 0-12-805456-5.
61. Brynn Hibbert, D.; Thordarson, P. The Death of the Job Plot, Transparency, Open Science and Online Tools, Uncertainty Estimation Methods and Other Developments in Supramolecular Chemistry Data Analysis. *Chem. Commun.* **2016**, *52*, 12792–12805. [[CrossRef](#)]
62. Neese, F. Software Update: The ORCA Program System—Version 5.0. *WIREs Comput. Mol. Sci.* **2022**, *12*, e1606. [[CrossRef](#)]
63. Grimme, S.; Hansen, A.; Ehlert, S.; Mewes, J.-M. R2SCAN-3c: A “Swiss Army Knife” Composite Electronic-Structure Method. *J. Chem. Phys.* **2021**, *154*, 064103. [[CrossRef](#)]
64. Takano, Y.; Houk, K.N. Benchmarking the Conductor-like Polarizable Continuum Model (CPCM) for Aqueous Solvation Free Energies of Neutral and Ionic Organic Molecules. *J. Chem. Theory Comput.* **2005**, *1*, 70–77. [[CrossRef](#)] [[PubMed](#)]
65. Allouche, A.-R. Gabedit—A Graphical User Interface for Computational Chemistry Softwares. *J. Comput. Chem.* **2011**, *32*, 174–182. [[CrossRef](#)] [[PubMed](#)]
66. Lu, T.; Chen, F. Multiwfn: A Multifunctional Wavefunction Analyzer. *J. Comput. Chem.* **2012**, *33*, 580–592. [[CrossRef](#)]
67. Humphrey, W.; Dalke, A.; Schulten, K. VMD: Visual Molecular Dynamics. *J. Mol. Graph.* **1996**, *14*, 33–38. [[CrossRef](#)]
68. Yanai, T.; Tew, D.P.; Handy, N.C. A New Hybrid Exchange–Correlation Functional Using the Coulomb-Attenuating Method (CAM-B3LYP). *Chem. Phys. Lett.* **2004**, *393*, 51–57. [[CrossRef](#)]
69. Rassolov, V.A.; Pople, J.A.; Ratner, M.A.; Windus, T.L. 6-31G\* Basis Set for Atoms K through Zn. *J. Chem. Phys.* **1998**, *109*, 1223–1229. [[CrossRef](#)]
70. Marsh, D.F.; Mink, L.M. Microscale Synthesis and Electronic Absorption Spectroscopy of Tetraphenylporphyrin  $\text{H}_2$ (TPP) and Metalloporphyrins  $\text{Zn}^{\text{II}}$ (TPP) and  $\text{Ni}^{\text{II}}$ (TPP). *J. Chem. Educ.* **1996**, *73*, 1188–1190. [[CrossRef](#)]

71. Lopes, J.M.S.; Sampaio, R.N.; Ito, A.S.; Batista, A.A.; Machado, A.E.H.; Araujo, P.T.; Neto, N.M.B. Evolution of Electronic and Vibronic Transitions in Metal(II) Meso-Tetra(4-Pyridyl)Porphyrins. *Spectrochim. Acta Part A Mol. Biomol. Spectrosc.* **2019**, *215*, 327–333. [[CrossRef](#)]
72. Edwards, L.; Dolphin, D.H.; Gouterman, M.; Adler, A.D. Porphyrins XVII. Vapor Absorption Spectra and Redox Reactions: Tetraphenylporphyrins and Porphin. *J. Mol. Spectrosc.* **1971**, *38*, 16–32. [[CrossRef](#)]
73. Khasanov, A.F.; Kopchuk, D.S.; Kovalev, I.S.; Taniya, O.S.; Giri, K.; Slepukhin, P.A.; Santra, S.; Rahman, M.; Majee, A.; Charushin, V.N.; et al. Extended Cavity Pyrene-Based Iptycenes for the Turn-off Fluorescence Detection of RDX and Common Nitroaromatic Explosives. *New J. Chem.* **2017**, *41*, 2309–2320. [[CrossRef](#)]
74. Mondal, T.; Mondal, I.; Biswas, S.; Mane, M.V.; Panja, S.S. Mechanistic Insight into Selective Sensing of Hazardous Hg<sup>2+</sup> and Explosive Picric Acid by Using a Pyrene-Azine-Hydroxyquinoline Framework in Differential Media. *ChemistrySelect* **2020**, *5*, 9336–9349. [[CrossRef](#)]
75. Santra, D.C.; Bera, M.K.; Sukul, P.K.; Malik, S. Charge-Transfer-Induced Fluorescence Quenching of Anthracene Derivatives and Selective Detection of Picric Acid. *Chem. A Eur. J.* **2016**, *22*, 2012–2019. [[CrossRef](#)]
76. Deshmukh, S.C.; Rana, S.; Shinde, S.V.; Dhara, B.; Ballav, N.; Talukdar, P. Selective Sensing of Metal Ions and Nitro Explosives by Efficient Switching of Excimer-to-Monomer Emission of an Amphiphilic Pyrene Derivative. *ACS Omega* **2016**, *1*, 371–377. [[CrossRef](#)]
77. Gole, B.; Bar, A.K.; Mukherjee, P.S. Fluorescent Metal–Organic Framework for Selective Sensing of Nitroaromatic Explosives. *Chem. Commun.* **2011**, *47*, 12137–12139. [[CrossRef](#)]
78. Ma, Y.; Li, H.; Peng, S.; Wang, L. Highly Selective and Sensitive Fluorescent Paper Sensor for Nitroaromatic Explosive Detection. *Anal. Chem.* **2012**, *84*, 8415–8421. [[CrossRef](#)]
79. Shanmugaraju, S.; Joshi, S.A.; Mukherjee, P.S. Fluorescence and Visual Sensing of Nitroaromatic Explosives Using Electron Rich Discrete Fluorophores. *J. Mater. Chem.* **2011**, *21*, 9130–9138. [[CrossRef](#)]
80. Ni, R.; Tong, R.B.; Guo, C.C.; Shen, G.L.; Yu, R.Q. An Anthracene/Porphyrin Dimer Fluorescence Energy Transfer Sensing System for Picric Acid. *Talanta* **2004**, *63*, 251–257. [[CrossRef](#)]
81. Gouterman, M. Optical Spectra and Electronic Structure of Porphyrins and Related Rings. In *The Porphyrins*; Dolphin, D., Ed.; Academic Press: Cambridge, MA, USA, 1978; pp. 1–165. ISBN 978-0-12-220103-5.
82. Wang, C.; Wamser, C.C. Hyperporphyrin Effects in the Spectroscopy of Protonated Porphyrins with 4-Aminophenyl and 4-Pyridyl Meso Substituents. *J. Phys. Chem. A* **2014**, *118*, 3605–3615. [[CrossRef](#)]
83. Wamser, C.C.; Ghosh, A. The Hyperporphyrin Concept: A Contemporary Perspective. *JACS Au* **2022**, *2*, 1543–1560. [[CrossRef](#)]
84. Vyšniauskas, A.; Qurashi, M.; Gallop, N.; Balaz, M.; Anderson, H.L.; Kuimova, M.K. Unravelling the Effect of Temperature on Viscosity-Sensitive Fluorescent Molecular Rotors. *Chem. Sci.* **2015**, *6*, 5773–5778. [[CrossRef](#)]
85. Miao, W.; Yu, C.; Hao, E.; Jiao, L. Functionalized BODIPYs as Fluorescent Molecular Rotors for Viscosity Detection. *Front. Chem.* **2019**, *7*, 825. [[CrossRef](#)] [[PubMed](#)]
86. Lee, S.-C.; Heo, J.; Woo, H.C.; Lee, J.-A.; Seo, Y.H.; Lee, C.-L.; Kim, S.; Kwon, O.-P. Fluorescent Molecular Rotors for Viscosity Sensors. *Chem. A Eur. J.* **2018**, *24*, 13706–13718. [[CrossRef](#)] [[PubMed](#)]
87. Hoche, J.; Schmitt, H.-C.; Humeniuk, A.; Fischer, I.; Mitrić, R.; Röhr, M.I.S. The Mechanism of Excimer Formation: An Experimental and Theoretical Study on the Pyrene Dimer. *Phys. Chem. Chem. Phys.* **2017**, *19*, 25002–25015. [[CrossRef](#)]
88. Kawai, T.; Ikegami, M.; Arai, T. Exciplex Formation between Pyrene and Guanine in Highly Polar Solvents. *Chem. Commun.* **2004**, *10*, 824–825. [[CrossRef](#)] [[PubMed](#)]
89. Hamada, F.; Narita, M.; Kinoshita, K.; Makabe, A.; Osa, T. Synthesis and Fluorescent Molecular Sensing at Exciplex Emission of Pyrene- and Cyanobenzene-Modified  $\gamma$ -Cyclodextrins. *J. Chem. Soc. Perkin Trans. 2* **2001**, *44*, 388–394. [[CrossRef](#)]
90. Bertocchi, M.J.; Zhang, X.-F.; Bajpai, A.; Moorthy, J.N.; Weiss, R.G. Fluorescence Quenching of Sterically-Graded Pyrene Molecules by N,N-Dialkylanilines. Exciplexes or Locally Excited States? *J. Photochem. Photobiol. A Chem.* **2018**, *355*, 467–478. [[CrossRef](#)]
91. Rasheed, T.; Nabeel, F.; Rizwan, K.; Bilal, M.; Hussain, T.; Shehzad, S.A. Conjugated Supramolecular Architectures as State-of-the-Art Materials in Detection and Remedial Measures of Nitro Based Compounds: A Review. *TrAC Trends Anal. Chem.* **2020**, *129*, 115958. [[CrossRef](#)]
92. Lewis, F.D.; Daublain, P.; Delos Santos, G.B.; Liu, W.; Asatryan, A.M.; Markarian, S.A.; Fiebig, T.; Raytchev, M.; Wang, Q. Dynamics and Mechanism of Bridge-Dependent Charge Separation in Pyrenylurea–Nitrobenzene  $\pi$ -Stacked Protophanes. *J. Am. Chem. Soc.* **2006**, *128*, 4792–4801. [[CrossRef](#)] [[PubMed](#)]
93. Johnson, E.R.; Keinan, S.; Mori-Sánchez, P.; Contreras-García, J.; Cohen, A.J.; Yang, W. Revealing Noncovalent Interactions. *J. Am. Chem. Soc.* **2010**, *132*, 6498–6506. [[CrossRef](#)]
94. Thordarson, P. Determining Association Constants from Titration Experiments in Supramolecular Chemistry. *Chem. Soc. Rev.* **2011**, *40*, 1305–1323. [[CrossRef](#)]

**Disclaimer/Publisher’s Note:** The statements, opinions and data contained in all publications are solely those of the individual author(s) and contributor(s) and not of MDPI and/or the editor(s). MDPI and/or the editor(s) disclaim responsibility for any injury to people or property resulting from any ideas, methods, instructions or products referred to in the content.